variables involved (such as uncertainties of constant velocity duration near the sun, a higher initial velocity, background solar wind velocity) to be justified for the purpose of this estimate.

The blast loading on an object is a function of both the incident blast wave characteristics (the peak overpressure, dynamic pressure and decay of pressure (drag) loading behind the shock) and of its duration. The overpressure on the front face can be found from dynamic shock-on-shock calculations (Fig. 6 of ref. 8) to be $P/P_T = 28$ for Mach 6 and a specific heat ratio of 5/3. Here, $P_T$ is the dynamic pressure at the stagnation point of the cometary object before impact. At 14.3 AU, this pressure is $\sim 10^{-10}$ dyn cm$^{-2}$. Hence the peak overpressure, which lasts for $\sim 2$ ms (see Fig. 5 of ref. 8 for a comparison of laboratory and numerical simulation results), is $\sim 3 \times 10^{-9}$ dyn cm$^{-2}$. The drag loading, after the peak pressure duration, is about half this value (again, see Fig. 6 of ref. 8) but lasts for many hours after shock propagation into the anti-solar direction. The initial impact loading $[3 \times 10^{-9}$ dyn cm$^{-2} \times \pi(6$ km$)^2]$ is $\sim 3,400$ dyn on the roughly hemispherical face of P/Halley. Experience with nuclear explosions shows that a visible (that is, apparent) crater is accompanied by a rupture zone and a plastic zone (Gladstone[14], Ch. VI). In the case of a fluffy amorphous icy crust on Halley (depth unknown), fissures, if not outright cracking, are possible. We are not aware of any published data on the compressive failure of fluffy amorphous ice at this low temperature ($-200$ °C). Associated with this scenario may be the heating suggested by Smoluchowski[15]. The temperature rise associated with the shock-on-shock impact would possibly cause some transformation from the amorphous to the crystalline state. Part of the impulsive pressure increase referred to above (a factor of 28) is due to the increase in density of the solar wind (a factor of 4). Thus, the combination of the temperature increase (a factor of 7) with the mechanical impact is likely to produce crystallization. The pressure of outflowing gases ($\sim 10^3$ dyn cm$^{-2}$) then dominates after the fissures occur[16].

Another issue to be addressed is whether there were comparable or greater increases in the solar wind pressure at the comet before December 1990–March 1991. These increases could have weakened the crust. We examined the available data on the solar wind from the Pioneer Venus Orbiter (PVO) from September 1990 to March 1991. In November 1990, PVO was at superior conjunction, and tracking of the spacecraft was therefore sparse. In addition, the competition for tracking was high from September to January, so that the tracking coverage of the spacecraft was low. Nevertheless, solar wind speeds are available on most days. From September to December 1990, the solar wind speed, as measured by the plasma analyser on PVO, was $\geqslant 600$ km s$^{-1}$ on only five occasions. From January to 10 April 1991, the speed was $\geqslant 600$ km s$^{-1}$ on nine occasions. During the latter period, PVO was located $\sim 180°$ away from comet Halley (see Fig. 1); nevertheless, these observations indicate that one or more strong flare-generated shock waves probably propagated outward through a quiescent solar wind and provided a strong enough impulse to cause the flaring of comet Halley. $\square$

1. Biermann, L. Z. Astrophys. 29, 274 (1951).
2. Parker, E. N. Interplanetary Dynamical Processes, 12–15 (Interscience, New York, 1963).
3. Nature 321, 280–368 (1986).
4. Proc. 20th ESLAB Symp. on the Exploration of Halley's Comet, ESA SP-250 (European Space Agency, 1986).
5. Nature 349, 732 (1991).
6. Levi, B. G. Physics Today 44, 20 (1991).
7. Intriligator, D. S. J. geophys. Res. 82, 603–617 (1977).
8. Dryer, M. Radio Sci. 8, 893–901 (1973).
9. Richter, N. B. Astr. Nachrichten 271, 207 (1941).
10. Dryer, M. et al. J. geophys. Res. 80, 2001–2012 (1975).
11. Smith, E. J. & Wolfe, J. H. Geophys. Res. Lett. 3, 137–140 (1976).
12. Weissman, P. R. ESA SP-250, 517–522 (1986).
13. Smart, D. F. & Shea, M. A. J. geophys. Res. 90, 183 (1985).
14. Glasstone, S. (ed.) The Effects of Nuclear Weapons, Ch. IV; Ch. VI (Superintendent of Documents, Washington DC, 1962).
15. Smoluchowski, R. Astrophys. J. 244, L31–L34 (1981).
16. Donn, B. & Rahe, J. in Comets (ed. Wilkening, L. L.), 203–226 (University of Arizona Press, Tucson, 1982).

# Structure and growth mechanism of mineral dendrites

## B. Chopard, H. J. Herrmann & T. Vicsek

HLRZ, KFA Jülich, Postfach 1913, 5170 Jülich, Germany

THE surfaces of limestones are often marked by black or red-brown deposits known as mineral dendrites[1,2]. These are deposits of hydrous iron or manganese oxides formed when supersaturated solutions of iron or manganese penetrate the limestone and are precipitated on exposure to air at the surface. Mineral dendrites have a fractal[3] appearance, but the origin and characteristics of this morphology, and its dependence on concentration gradients or reaction rates have been little studied. Here we analyse the shapes and fractal properties of mineral dendrites from several different origins, and propose a lattice reaction–diffusion model for their formation. The model shows how different reaction conditions can account for the variation in fractal dimension observed in real dendrites.

Mineral dendrites are distinct from the 'dendritic' crystal morphologies obtained by solidification from an undercooled melt, the understanding of which is fairly well developed[4,5]. Mineral dendrites are formed by an irreversible chemical reaction and have an appearance similar to the clusters of diffusion-limited aggregation (Fig. 1) rather than the branched form of 'dendritic growth'[4,5].

We collected samples of mineral dendrites from various parts of the world and photographed them. For those samples with good contrast, we digitized the pictures with a resolution $720 \times 600$ and analysed them using the sand-box technique[6] to calculate the fractal dimension. This method is based on determining the mass $M$ (the number of occupied pixels of the digitized image) within square boxes of varying size centred at points randomly selected on the fractal pattern. The fractal dimension $d_f$ is obtained from the expression $M(r) \propto r^{d_f}$, where $M(r)$ is the average mass in boxes of linear size $r$. We selected 2,000 centres for each picture.

The results for three different samples are shown in Fig. 1. The first sample, from Bavaria (Fig. 1a), consists of particularly well-developed, densely packed long branches which can be distinguished with a resolution of $<0.1$ mm. The second sample, from Greece (Fig. 1b), shows more common, shorter, but also fairly densely packed dendrites emerging from cracks in limestone. For both Fig. 1a and 1b, results are shown for two different samples from the same location. If the mass within a box is plotted logarithmically against the size of the box (left-hand side of Fig. 1), we find straight lines of non-integer slope over about two orders of magnitude, showing that the patterns are fractal. The fractal dimension $d_f$ can be read off and we find for the first two samples $d_f = 1.78 \pm 0.04$. In the third sample, from Brazil (Fig. 1c) the dendrite is an inclusion within the plane of a crack inside a quartz crystal. There is only one dendrite, probably because there was a single injection hole. It is less dense, but is fractal, and the fractal dimension obtained from the figure is $d_f = 1.51 \pm 0.05$. We have analysed in this way other samples with finger widths (length scale) ranging from one-tenth to several millimetres. All are fractal. Those on limestone are dense, with fractal dimensions of $\sim 1.78$; in quartz, their fractal dimension is lower.

To explain the dendritic structures, we will mimic the chemical process of manganese ions diffusing out of cracks and oxidizing in the reaction: $Mn^{4+} + 2O^{2-} \rightarrow MNO_2$. For this we devised the following reaction–diffusion model. We consider two species of particles, A and B, which diffuse on a square lattice. When an A and a B particle are simultaneously on the same site, they react forming C ($A + B \rightarrow C$). The C particles also diffuse until they precipitate into D ($kC \searrow D$). The D particles are stationary, and the sites where they are created will be marked black for

all successive time-steps (see Fig. 2a–c).

Two conditions will lead C to transform into D: first, when at least $k$ particles of type C simultaneously meet on the same site, saturation occurs, and the C particles precipitate to form D; second, when a C particle becomes nearest neighbour to a black site D, it aggregates to the cluster.

Such a reaction–diffusion process will cause a reaction front to build up if the A and B species are initially separated in space. If the concentrations of A and B ($\rho_A$ and $\rho_B$) are different, this reaction front moves across the system, leaving clusters of D particles in its wake. The values of $\rho_A$ and $\rho_B$ play a crucial part in the dynamics, as they determine the concentration of C particles produced in the reaction zone and the speed of the front (which moves faster as the concentration difference increases).

Because of the motion of the front, the clusters grow asymmetrically. Their density depends on the amount of C released by the A–B reaction. If the rate at which C particles aggregate is not too large compared with the rate at which they are produced, long and continuous clusters are formed along the direction of motion of the front. On the other hand, if the C particles are produced too slowly and the front moves fast enough, the cluster growth will die out rapidly because all the C available at a given time and position will be exhausted by aggregation. To create a new cluster, one has to wait until spontaneous precipitation occurs ($kC \searrow D$), which requires a
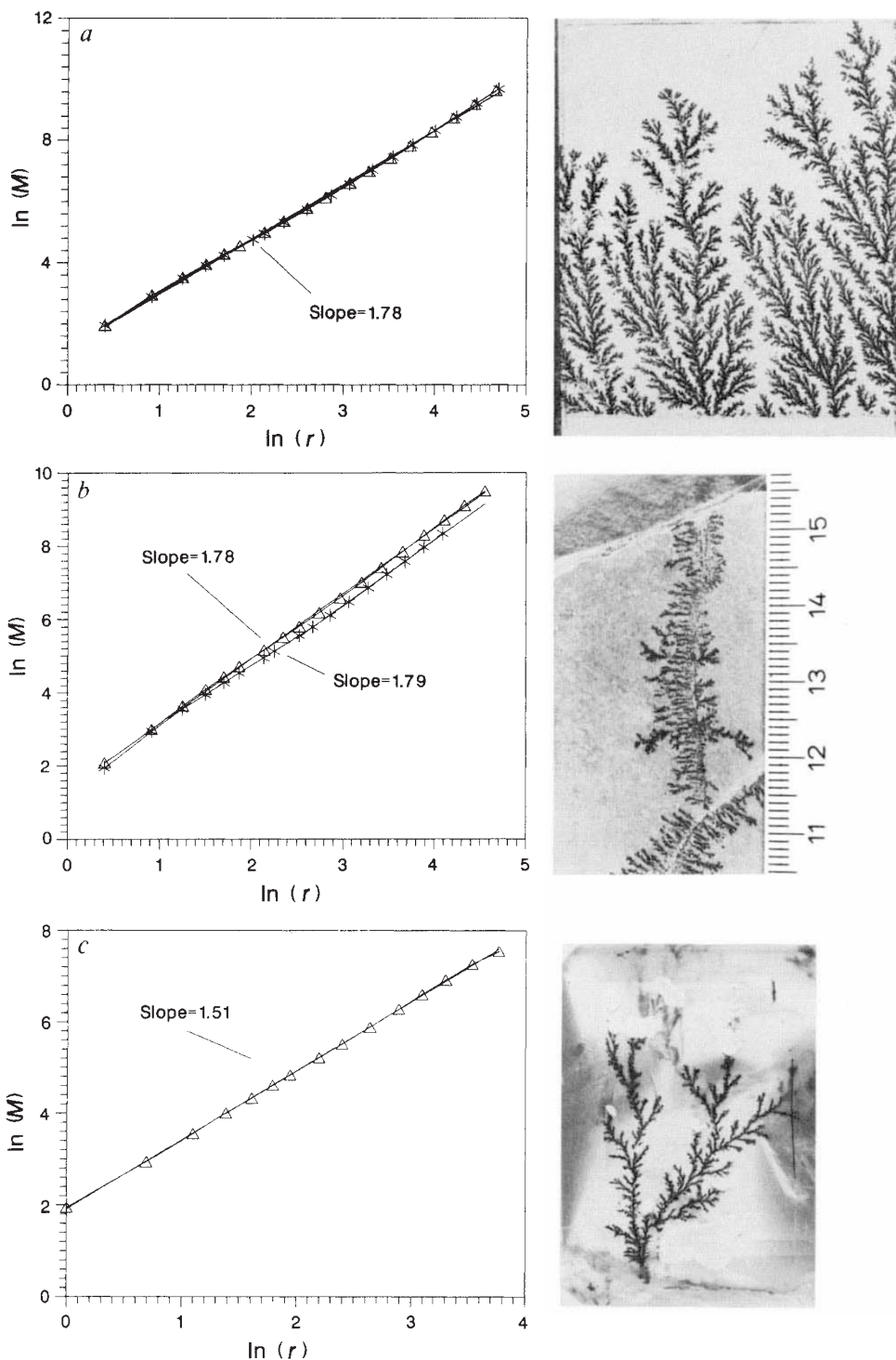


FIG. 1 Photographs of various manganese oxide mineral dendrites (left) and the log–log plots (natural logarithm) of their mass as function of the length of the box (right) for a, Solnhofener Kalkstein, Bavaria; b, limestone from Corfu, Greece and c, inclusions in quartz from Ouro Preto, Brazil.

large enough concentration of C. This is likely to happen after the reaction $A + B \rightarrow C$ has run for a while, that is at some position further away. This gives rise to small and isolated clusters.

The numerical simulation is set up on a two-dimensional square lattice, with periodic boundary conditions in the horizontal direction. The system is initially filled with a concentration $\rho_A = 1$ of A particles on the lower part and a concentration $\rho_B \ll 1$ of B particles on the upper part. On the bottom line, there is a source of A particles with a concentration of 1: on each site, any particle that leaves is immediately replaced by a new one. On the top line, a source of B with concentration $\rho_B$ is similarly imposed. We chose $k = 4$ as the number of C particles needed to form a precipitate.

Because of the externally imposed concentration gradient $\rho_A \gg \rho_B$, the reaction front moves upward leaving behind it a tree-like pattern. The smaller the concentration $\rho_B$, the faster the reaction front moves and the less dense are the precipitate clusters left behind, as seen by comparing Fig. 2a ($\rho_B = 1/20$) with Fig. 2c ($\rho_B = 1/50$). In Fig. 2b, we put straight lines of precipitate into the lattice by hand before starting the diffusion process, to mimic the fracture lines seen in Fig. 1b. The structures of Fig. 2a-c strongly resemble the pictures in the corresponding Fig. 1a-c, indicating that our reaction–diffusion model describes the formation of mineral dendrites fairly well. A similar reaction–diffusion scheme is also believed to be responsible for the formation of the 'Liesegang bands'[7,8]. Although some features of these bands are captured by our model, the time and length scale are not appropriate.

Our numerical algorithm is of cellular automaton type. It is well suited for a vector computer or a massively parallel architecture. Our simulations were conducted both on a CRAY–YMP and a 16-K Connection Machine. The simulations were run for $\sim 10^5$ time steps, over a lattice of $512 \times 512$ sites. Only a fraction of the total size ($\sim 1/4$ and $1/8$) is shown in Fig. 2. The speed of the algorithm is $\sim 2 \times 10^7$ updates per second, on both machines.

We next analyse the fractal dimension of our cluster. We use the sand-box method by placing concentric boxes, of linear size 2–20 lattice sites, so that they are centred around sites of the precipitate (see Fig. 2a-c). A log–log plot of the mass inside a box (number of black sites) as a function of its size produces the straight lines shown in Fig. 2d, f and g, corresponding to the clusters of Fig. 2a, b and c, respectively. In the high-density cases, where $\rho_B = 1/20$ (Fig. 2d and f), we find $d_f = 1.76$, whereas $\rho = 1/50$ gives the lower value of 1.58 (Fig. 2g). To check the reliability of the method, we also analysed the pattern of Fig. 2a using box-counting[6]: we placed grids of different lattice sizes over the system and counted for each size the number of boxes that are not empty. A log–log plot of these data should give a straight line with slope $-d_f$. The results are shown in Fig. 2e; when the smallest boxes are excluded, the value of $d_f$ obtained in this way is consistent with that obtained from the sand-box method.

The fractal dimensions calculated from our numerical model agree well with those obtained from the analysis of real mineral dendrites. We conclude from this that the model describes the essential features of the process underlying the formation of dendrites in nature: diffusion, with a reaction front and irreversible aggregation. These elements are also responsible for the formation of fractals in electrodeposition of zinc leaves[9] and other experimental applications of diffusion-limited aggregation (DLA)[10]. But DLA in its original form cannot explain all features of mineral dendrites. First, we know that in our case the chemistry is more complex, and the existence of at least three species has to be considered. Second, the observed dendrites have varying fractal dimensions, whereas DLA results in a unique value $D \approx 1.70$. Our process is similar to reaction-limited aggregation with the difference that in our case the reaction takes place in a moving front.

We conclude that on a certain length scale, mineral dendrites

are fractal, and that this effect can be explained by a reaction–diffusion–aggregation model which has similarities to other laplacian growth models that produce fractals[6]. The range over which the dendrites are fractal is limited from below by the finger width and from above by the size of a tree and covers easily two orders of magnitude. In this sense our fractal dimensions are only effective exponents, and their value depends on the density of the precipitate. For the more typical case of manganese on limestone, a dimension of $\sim 1.75$ is found, whereas inclusions in crystals have lower values. Probably these exponents can be explained as a crossover behaviour towards the critical case of infinitely large clusters. Although the numerically obtained pictures are very similar to the photographs of
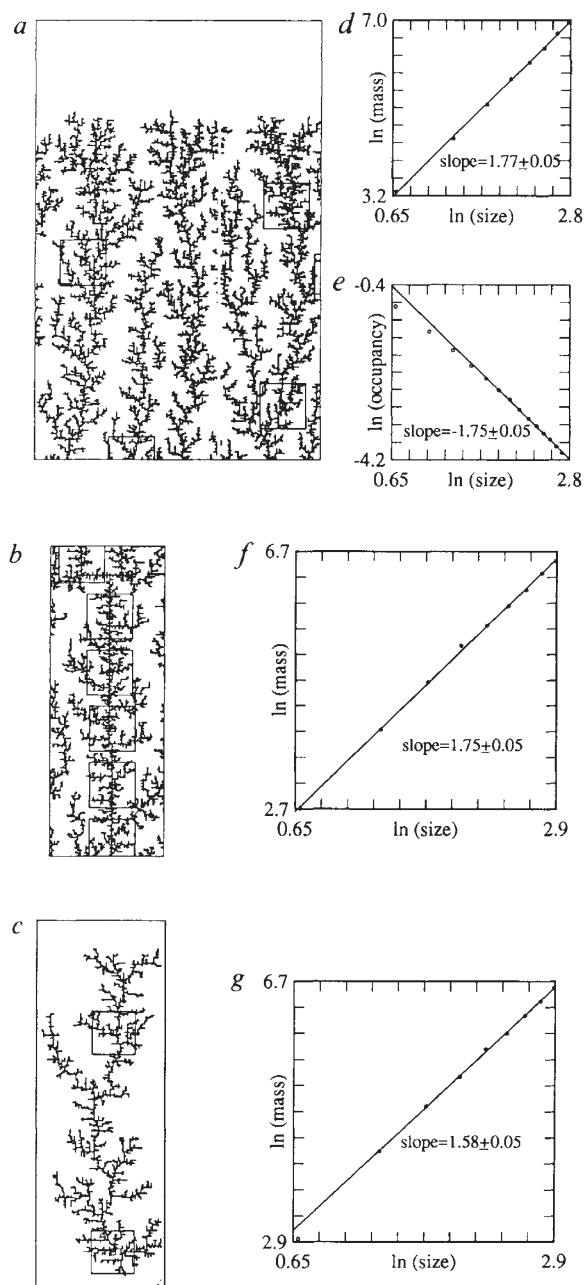


FIG. 2 Numerical results from the reaction–diffusion model. The initial concentration of B is $\rho_B = 1/20$ in a and b, and 1/50 in c. The measurement of the fractal dimension with the sand-box method is shown in d, f and g for the clusters obtained in a, b and c, respectively. The square boxes in a, b and c show the maximum box size used for this measurement. The results of a box-counting method for a are given in e. Only the data shown as black dots have been taken into account in the least-squares fit.

mineral dendrites, the underlying square lattice is still recognizable in the simulated precipitates. Therefore, off-lattice simulations would be interesting. □

1. Bates, R. L. & Jackson, J. A. (ed.) *Glossary of Geology* (American Geological Institute, Alexandria, 1987).
2. Loewinson-Lessing, F. & Macdonald, G. A. *Bull. US Geol. Surv.* **994**, 42–44 (1953).
3. Mandelbrot, B. *The Fractal Geometry of Nature* (Freeman, San Fransisco, 1982).
4. Ben-Jacob, E. & Garik, P. *Nature* **343**, 523–530 (1990).
5. Langer, J. S. *Science* **243**, 1150–1155 (1989).
6. Vicsek, T. *Fractal Growth Phenomena* (World Scientific, Singapore, 1989).
7. Dee, G. T. *Phys. Rev. Lett.* **57**, 275–278 (1986).
8. Liesegang, R. E. *Naturwissenschaften Wochenschr.* **11**, 353–362 (1896).
9. Matsushita, M., Sano, M., Hayakawa, Y., Honjo, H. & Sawada, Y. *Phys. Rev. Lett.* **53**, 286–289 (1984).
10. Witten, T. A. & Sander, L. M. *Phys. Rev. Lett.* **47**, 1400–1403 (1981).

# Spatial orientation of molecules in strong electric fields and evidence for pendular states

**Bretislav Friedrich & Dudley R. Herschbach**

Department of Chemistry, Harvard University, Cambridge, Massachusetts 02138, USA

IN typical collisional or spectroscopic experiments, molecules rotate freely with random spatial orientations. The resulting isotropic averaging obscures or suppresses much stereodynamical information and has remained a recalcitrant problem. The only practical means for orienting a molecule itself, rather than just its axis of rotation, has been electric field focusing[1,2]. But this is applicable only to certain rotational states of symmetric top molecules (or equivalent) that exhibit a first-order Stark effect. Orientation of molecules other than symmetric tops has long been considered to be quite unfeasible[3]. Recently, however, it has been pointed out[4,5] that by exploiting the extreme rotational cooling that can occur in supersonic molecular beams, substantial orientation of diatomic, linear or asymmetric top molecules should become possible at accessible field strengths. The anisotropy of the Stark effect allows molecules in the lowest few rotational states to be trapped in 'pendular states' and thereby confined to librate (oscillate about the field axis) over a limited angular range. Here we describe an experiment which demonstrates that oriented pendular states can be obtained for a diatomic molecule with modest field strengths. With anticipated improvements, this technique should become widely applicable.

The ability to orient symmetric top molecules has enabled studies to be carried out to probe the anisotropic forces governing collisions with reactive atoms[6–8], photons[9] or surfaces[10]. In contrast to symmetric tops, however, which in the orientable states precess about the field vector, diatomic, linear or asymmetric top molecules tumble in all rotational states. This averages out the dipole moment in first order and hence greatly weakens interaction with an electric field. Typically, for a gas at room temperature, the interaction energy of the dipole moment with a feasible electric field is only $\sim 0.1$–1% of the mean rotational energy. Thus despite the presence of the field, all but a very small fraction of the molecules continue rotating like pinwheels.

A molecular beam formed by supersonic expansion offers a great advantage (see ref. 11 and refs therein) as collisional relaxation can drop the rotational temperature down to 1 K or less. Theoretical calculations[4,5] show that for many polar molecules, such cooling should permit a large fraction of the beam molecules to be considerably oriented without need for inordinately large field strengths. The cooling condenses much of the beam population into the lowest few rotational states.

These can be converted from pinwheeling to pendular states simply by sending the beam into a region subject to a strong uniform electric field. For most prospective applications, this region can be quite small; there is no need for the long focusing fields used to select the orientable states of symmetric tops.

In our experiment a molecular beam containing $\sim 15$–20% ICl seeded in $H_2$ is formed by expanding the gas mixture at 110 torr and 310 K through a glass nozzle 250 μm in diameter. The beam passes between a pair of parallel plate electrodes, 2 cm long, 2 cm wide and 1.7 cm apart, fashioned either from metal grids or from conducting glass (a glass with a conducting transparent layer of fluorine-doped $SnO_2$ was provided by R. Gordon). In the gap between these electrodes, the molecules are subject to a static electric field which could be scanned up to 20 kV cm$^{-1}$. The molecular beam within the gap is illuminated with orange-red light from a pulsed dye laser (Lambda Physik, EMG 202/FL 3002E). By scanning the laser wavelength, we observe an excitation spectrum with resolved rotational structure. This is detected by a photomultiplier (RCA C31034A) which views the accompanying optical fluorescence through one of the electrodes. Active background subtraction and gating of the photon counters is used to enhance the signal-to-background ratio. The field-induced shifts in rotational line positions and intensities provide the means to characterize the extent of molecular orientation achieved.

Figure 1 shows examples of laser-induced fluorescence spectra, illustrating striking changes in the rotational structure with the field strength. The particular vibronic band of I$^{35}$Cl was chosen for study because of its favourable Franck–Condon factors and little overlap by lines from $I_2$ contamination in the beam. Accurate spectroscopic constants are well established[12] for the ground electronic state, X $^1\Sigma^+$. Less accurate constants, including the dipole moment, are also available for the A $^3\Pi$ excited electronic state from the work of Cummings and Klemperer[13] and others[14–16]. We obtained spectral assignments and values of the dipole moment $\mu'$ and rotational constant $B'$ consistent with their results.

Figure 2 compares the lowest few energy levels[17] and transitions with (left) and without (right) the electric field. The states are labelled with quantum numbers $J$, $M$, designating the rotational angular momentum and its projection on the field direction. Transitions are labelled in the usual fashion (see Fig. 1). We also plot (left) the potential energy, given by $-\mu\varepsilon\cos\theta$, for a dipole moment $\mu$ in an electric field of strength $\varepsilon$, with $\theta$ the angle between the dipole axis and the field direction. The energy levels bound within the cosine potential correspond to pendular states. These states are hybrids of the field-free rotational states[18,19], comprising linear combinations of spherical harmonics with a range of $J$ but the same fixed value of $M$. With increasing field strength, the range of $J$ contributing to a pendular state expands as the state is drawn down lower in the cosine potential and its librational amplitude narrows.

For the ICl spectra examined here, the dipole moment of the excited electronic state A $^3\Pi$ is similar in magnitude but suspected[13] to be opposite in sign to that for the ground state, X $^1\Sigma^+$. Reversing the sign of the dipole does not change the energy levels but is equivalent to shifting the cosine potential by $\theta \to \theta + 180°$. This is advantageous for our purpose. For example, if the laser-induced excitation of an ICl molecule occurs with $\theta \approx 0°$, this will correspond to the most attractive region of the potential well for the ground state X but to the most repulsive region for the excited A state. Accordingly, the excitation probability for a rotational transition such as $R_{00}$, corresponding to $0, 0(X) \to 1, 0(A)$, will depend on the exponentially decaying tail of the $1, 0(A)$ wavefunction in the classically excluded region, once the field strength becomes large enough to ensure that both $0, 0(X)$ and $1, 0(A)$ are pendular states. This makes the intensity of such transitions extremely sensitive to the librational amplitude.